NASA/TM—2014-218338

Multilayer Thermal Barrier Coating (TBC) Architectures Utilizing Rare Earth Doped YSZ and Rare Earth Pyrochlores

Michael P. Schmitt
The Pennsylvania State University, University Park, Pennsylvania

Amarendra K. Rai and Rabi Bhattacharya
UES Inc., Dayton, Ohio

Dongming Zhu
Glenn Research Center, Cleveland, Ohio

Douglas E. Wolfe
The Pennsylvania State University, University Park, Pennsylvania

July 2014

NASA STI Program . . . in Profile

Since its founding, NASA has been dedicated to the advancement of aeronautics and space science. The NASA Scientific and Technical Information (STI) program plays a key part in helping NASA maintain this important role.

The NASA STI Program operates under the auspices of the Agency Chief Information Officer. It collects, organizes, provides for archiving, and disseminates NASA's STI. The NASA STI program provides access to the NASA Aeronautics and Space Database and its public interface, the NASA Technical Reports Server, thus providing one of the largest collections of aeronautical and space science STI in the world. Results are published in both non-NASA channels and by NASA in the NASA STI Report Series, which includes the following report types:

- TECHNICAL PUBLICATION. Reports of completed research or a major significant phase of research that present the results of NASA programs and include extensive data or theoretical analysis. Includes compilations of significant scientific and technical data and information deemed to be of continuing reference value. NASA counterpart of peer-reviewed formal professional papers but has less stringent limitations on manuscript length and extent of graphic presentations.

- TECHNICAL MEMORANDUM. Scientific and technical findings that are preliminary or of specialized interest, e.g., quick release reports, working papers, and bibliographies that contain minimal annotation. Does not contain extensive analysis.

- CONTRACTOR REPORT. Scientific and technical findings by NASA-sponsored contractors and grantees.

- CONFERENCE PUBLICATION. Collected papers from scientific and technical conferences, symposia, seminars, or other meetings sponsored or cosponsored by NASA.

- SPECIAL PUBLICATION. Scientific, technical, or historical information from NASA programs, projects, and missions, often concerned with subjects having substantial public interest.

- TECHNICAL TRANSLATION. English-language translations of foreign scientific and technical material pertinent to NASA's mission.

Specialized services also include creating custom thesauri, building customized databases, organizing and publishing research results.

For more information about the NASA STI program, see the following:

- Access the NASA STI program home page at *http://www.sti.nasa.gov*

- E-mail your question to *help@sti.nasa.gov*

- Fax your question to the NASA STI Information Desk at 443–757–5803

- Phone the NASA STI Information Desk at 443–757–5802

- Write to:
  STI Information Desk
  NASA Center for AeroSpace Information
  7115 Standard Drive
  Hanover, MD 21076–1320

NASA/TM—2014-218338

Multilayer Thermal Barrier Coating (TBC)
Architectures Utilizing Rare Earth Doped YSZ
and Rare Earth Pyrochlores

Michael P. Schmitt
The Pennsylvania State University, University Park, Pennsylvania

Amarendra K. Rai and Rabi Bhattacharya
UES Inc., Dayton, Ohio

Dongming Zhu
Glenn Research Center, Cleveland, Ohio

Douglas E. Wolfe
The Pennsylvania State University, University Park, Pennsylvania

National Aeronautics and
Space Administration

Glenn Research Center
Cleveland, Ohio 44135

July 2014

Acknowledgments

Level of Review: This material has been technically reviewed by technical management.

Available from

Multilayer Thermal Barrier Coating (TBC) Architectures Utilizing Rare Earth Doped YSZ and Rare Earth Pyrochlores

Michael P. Schmitt
The Pennsylvania State University
University Park, Pennsylvania 16802

Amarendra K. Rai and Rabi Bhattacharya
UES Inc.
Dayton, Ohio 45432

Dongming Zhu
National Aeronautics and Space Administration
Glenn Research Center
Cleveland, Ohio 44135

Douglas E. Wolfe
The Pennsylvania State University
University Park, Pennsylvania 16802

Abstract

To allow for increased gas turbine efficiencies, new insulating thermal barrier coatings (TBCs) must be developed to protect the underlying metallic components from higher operating temperatures. This work focused on using rare earth doped (Yb and Gd) yttria stabilized zirconia (t' Low-k) and $Gd_2Zr_2O_7$ pyrochlores (GZO) combined with novel nanolayered and thick layered microstructures to enable operation beyond the 1200 °C stability limit of current 7 wt% yttria stabilized zirconia (7YSZ) coatings. It was observed that the layered system can reduce the thermal conductivity by ~45 percent with respect to YSZ after 20 hr of testing at 1316 °C. The erosion rate of GZO is shown to be an order to magnitude higher than YSZ and t' Low-k, but this can be reduced by almost 57 percent when utilizing a nanolayered structure. Lastly, the thermal instability of the layered system is investigated and thought is given to optimization of layer thickness.

Introduction

As the push continues for higher operating temperatures in gas turbines, research into advanced thermal barrier coatings (TBCs) has become increasingly important. A typical TBC system is composed of a 7 wt% yttria stabilized zirconia (7YSZ) insulating porous ceramic top coat which is deposited onto a bond coated nickel based superalloy (Ref. 1). 7YSZ is chosen due to its relatively low thermal conductivity, high thermal expansion coefficient and high erosion resistance. The bond coat of choice is usually a Pt modified nickel aluminide, (Pt,Ni)Al, though recent interest has been focused on γ/γ' type coatings (Refs. 2 and 3). Since the top coat 7YSZ material is a very good oxygen conductor, the bond coat serves to form a stable, slow growing and mechanically robust thermally grown oxide or TGO, typically α-Al_2O_3. This TGO protects the underlying substrate from severe oxidation which could produce spinels and/or other unwanted and poorly adherent oxides, thus resulting in enhanced TBC adhesion.

The primary focus for the development of advanced TBCs is reducing the thermal conduction through the TBC system while maintaining thermo-mechanical and thermo-chemical stability. Current 7YSZ thermal barriers are inadequate due to their elevated temperature phase instability (>1200 °C), increased sintering rate and inadequate thermal conductivity. Thus the insulating ceramic top coat of next generation TBCs must possess lower thermal conductivity and sintering rates than 7YSZ, while

maintaining erosion resistance and phase stability at elevated (>1400 °C) temperatures. Co-doped YSZ and the rare earth zirconate pyrochlores have garnered attention as potential replacements of 7YSZ (Refs. 1, 4 to 7). YSZ co-doped with rare earths have shown substantially lower thermal conductivities and sintering rates than 7YSZ (Ref. 7). Zhu et al. (Ref. 5) ascribed this to the formation of immobile defect clusters which efficiently scatter phonons while substantially hindering diffusion. The second class of plausible replacement coatings are the pyrochlore type rare earth zirconates, $RE_2Zr_2O_7$ (Ref. 4). These materials possess phase stability from 1500 °C to over 2000 °C while exhibiting thermal conductivities and sintering rates significantly lower than 7YSZ. Additionally, researchers (Ref. 8) have indicated a beneficial reduction in CMAS degradation with $Gd_2Zr_2O_7$. The primary drawback of rare earth zirconates is a requirement for a diffusion barrier to prevent reactions with the TGO (Ref. 9) and a low toughness which results in a significant reduction in the erosion performance compared to standard 7YSZ.

This study investigates rare earth doped YSZ (ZrO_2: 2mol% Y_2O_3 + 1mol% Yb_2O_3 + 1mol% Gd_2O_3) and the rare earth pyrochlore $Gd_2Zr_2O_7$ as possible replacements for 7YSZ. Herein referred to as t' Low-k and GZO respectively, these materials possess both lower thermal conductivity and sintering rates than 7YSZ. As the relatively high erosion rate of monolithic GZO could prove too large to adapt it into a reliable coating, unique multilayer architectures have been deposited in order to reduce the erosion rate relative to GZO while maintaining superior thermal conductivity over 7YSZ.

Experimental Procedure

One inch diameter (Pt,Ni)Al bond coated (Alcoa Howmet, Whitehall MI) Rene N5 (Sophisticated Alloys, Butler PA) buttons were used as substrate materials. For high temperature isothermal heat treatment work, 1 by 1 in. polycrystalline Al_2O_3 substrates (CoorsTek, 99.5 percent pure) were also utilized. The various coating architectures and compositions can be found in Table 1. Monolayer TBC structures of 7YSZ, t' Low-k and GZO (M1, M2, and M3, respectively) were deposited onto substrates via electron beam-physical vapor deposition (EB-PVD). A source-substrate distance of 12 in. was maintained while substrates rotated at 7 rpm on a 2 in. diameter mandrel directly above the ingot material. The multilayered TBC structures from M4 and M5 were fabricated by depositing alternating layers of t' Low k and GZO. For M4, the necessary ingots were co-evaporated and a vapor shield was used to prevent intermixing of the vapor clouds. Rotation through each vapor cloud provided a coating with alternating layers of t' Low-k and GZO at an average individual layer thicknesses of ~200 nm. In the case of M5, the electron beam was alternated between two ingots, thus only a single ingot was evaporated at a time. This technique yielded layered coatings with individual layer thicknesses on the order of ~30 μm. The overall thickness of M1-M3 was ~200 μm, while M4 and M5 were slightly thicker at around 300 μm. Prior to the deposition of M3-M5, a ~25 μm diffusion barrier layer of YSZ (M3) or t'-Low k (M4-M5) was deposited on top of the bond coat to maintain thermochemical stability between GZO and the TGO. A detailed description of the coating deposition procedure is described in Reference 10.

Thermal conductivity of the as-fabricated TBCs was measured at the NASA Glenn Research Center via a steady-state heat flux technique. Pass through heat flux and the measured temperature gradients through the ceramic coating system were used in conjunction with a one-dimensional heat transfer model to calculate the thermal conductivity (Ref. 11). Briefly, the TBC surface temperature was maintained at

TABLE 1.—DEPOSITION MATRIX DETAILING THE COATING, COMPOSITION AND STRUCTURE FOR
THE SINGLE LAYER AND MULTILAYER COATINGS USED IN THIS STUDY

Matrix #	Coating	Composition	Design architecture
M1	7YSZ	ZrO_2: $4Y_2O_3$ (mol%)	Monolayer
M2	t' Low-k	ZrO_2: $2Y_2O_3$ + $1Yb_2O_3$ + $1Gd_2O_3$ (mol%)	Monolayer
M3	GZO	$Gd_2Zr_2O_7$	Monolayer
M4	t' Low-k/GZO	ZrO_2: $2Y_2O_3$ + $1Yb_2O_3$ + $1Gd_2O_3$ (mol%)/$Gd_2Zr_2O_7$	Nanolayer
M5	t' Low-k/GZO	ZrO_2: $2Y_2O_3$ + $1Yb_2O_3$ + $1Gd_2O_3$ (mol%)/$Gd_2Zr_2O_7$	Thick layer

1316 °C for 20 hr through a constant heat flux from a 3.0 kW CO_2 laser while backside air cooling was used to maintain the desired thermal gradient and specimen temperature. Surface and backside temperatures were measured via optical pyrometers while a laser reflectometer measured the reflection loss at the surface. A laser delivered heat flux was calibrated using a sample of known thermal conductivity and by subtracting the laser reflection loss at the surface from the known heat flux, the pass through heat flux can be determined. The pass-through heat flux was further verified experimentally. The TBC/metal interface temperature was obtained using the known thermal conductivity of Rene N5 metal substrate. The overall thermal conductivity as functions of coating thickness, temperature and testing time was determined from the heat fluxes and the corresponding temperature gradients across the ceramic coating. Further details of the thermal conductivity measurement procedure are given elsewhere (Refs. 11 and 12).

Particle erosion was performed using an in-house erosion rig. TBC specimens were weighed and mounted into the sample holder with a 0.5 in. mask. The sample holder was then loaded into the erosion rig directly beneath the particle acceleration tube which ensured consistency through all the erosion trials and also allowed for adjustable incident angle of erodent. After mounting, the rig was calibrated and a measured amount of media was placed into the feeder trough. In this study, the dosage increment was 5 g of 240 grit (50 μm) Al_2O_3 and it was fed at a rate of ~2 g/min for a total of ~2.5 min. During testing, a vibratory feed system feeds the powder from the trough into the acceleration tube, where compressed air accelerates the erosion particles. Air pressures of 30 psi were used to accelerate particles to speeds of 100 m/s at incident angles of 90°. After one 'dose' the samples were weighed again to measure weight loss and the process was repeated. Weight loss was then plotted as a function of erodent fed and the coatings were eroded until sufficient data points were present to determine an erosion rate.

X-ray diffraction (PANalytical Empyrean) and Jade 10 software were used to characterize the crystallography in all the samples. Scanning electron microscopy (FEI Quanta 2000) was used to characterize the microstructure in the as deposited state and after erosion testing while box furnaces were used to carry out the high temperature anneals.

Results and Discussion

Monolayer Coatings

The as deposited cross sections of the single phase TBCs from M1-M3 are shown in Figures 1(a) to (c), respectively. The columnar morphology is clearly present in all three coatings. M1 and M2 appear to have slightly smaller column diameters than M3 whose columns appear slightly more feathered. The diffraction patterns for coatings M1-M5 are presented in Figure 2. The tetragonal splitting of the (004) to (400) peaks of M1 and M2 is visible at values of ~73.2 and ~74.2 °2θ, respectively. M3 exhibits a single peak at 71.9 °2θ, indicative of a cubic phase. All of the single layer coatings were textured with their highest intensity peaks corresponding to the {311} planes.
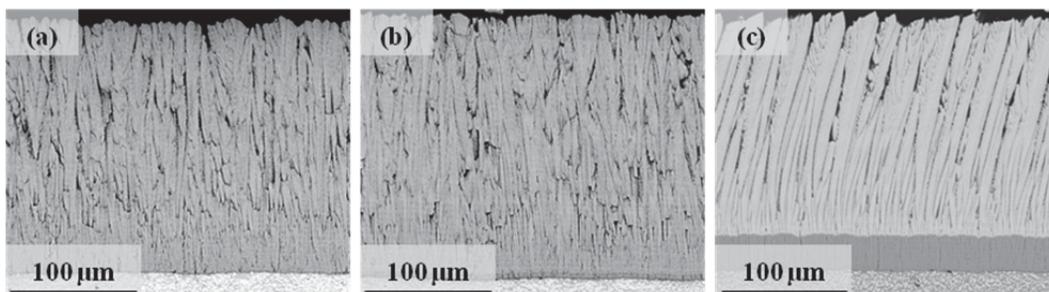
Figure 1.—SEM images of the polished cross sections of as deposited (a) M1 - YSZ, (b) M2 - t' Low-k, (c) M3 - GZO. Note that M3 also includes a ~25 μm t' Low-k diffusion barrier.
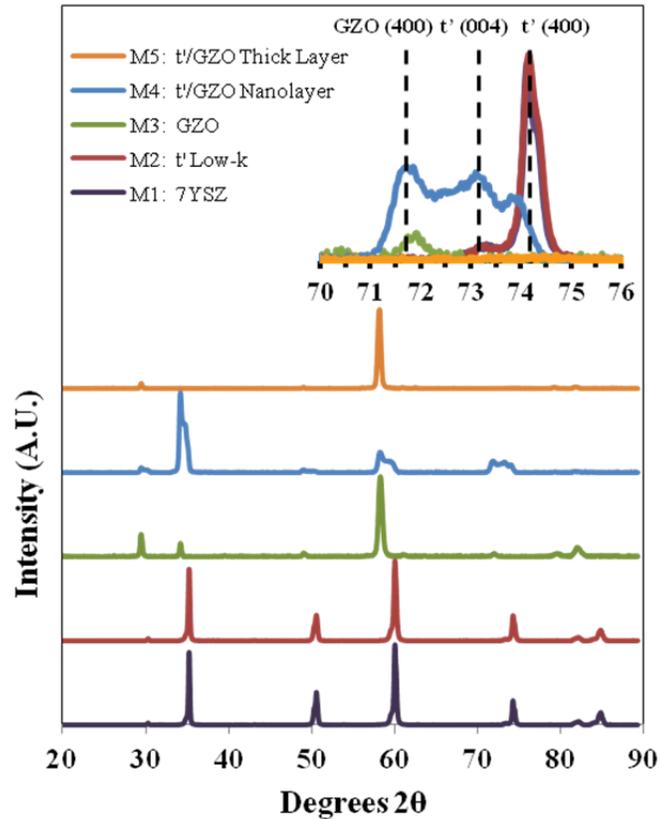
Figure 2.—X-ray diffraction patterns of as deposited M1-M5 with the high angle (004)/(400) region inset. The mixed phase nature of nanolayer M4 is clearly evident.

The thermal conductivities of M1-M5 are presented in Figure 3. The chart displays the initial thermal conductivity in the darker shade with the final thermal conductivity after 20 hr of testing at 1316 °C in the lighter shade. This allows the sintering rates of the coatings to be examined which is important as sintering not only leads to increased thermal conductivity but also reduced mechanical performance. The initial thermal conductivity of M1 was 1.45 W/m-K and increased by 52 percent to 2.2 W/m-K after 20 hr. The addition of rare earths in the M2 coating decreased the initial thermal conductivity to 1.2 W/m-K with only a 37 percent increase to 1.64 W/m-K after 20 hr. The decreased sintering rate indicates these coatings are significantly more stable, both microstructuraly and chemically, than standard 7YSZ coatings in M1. This is very important, since sintering of the columns leads to increased erosion while also reducing strain tolerance, and thus thermal cyclic life. The GZO coating from M3 has the lowest thermal conductivity of the three compositions, with an initial conductivity of 1.13 W/m-k and a small increase of 26 percent to 1.42 W/m-k after 20 hr. This is a substantial decrease from M1, whose initial thermal conductivity is even greater than the sintered value of GZO. This value could be further reduced by increasing coating porosity, but at the expense of erosion performance. The sintering rate of M3 is also about half that of M1, and about three fourths that of M2. This suggests the GZO coating would have less column sintering through its lifetime, and thus minimal increases in erosion rate through its lifetime. From these results, it is clear that M3 (GZO) is significantly more stable at high temperatures (1316 °C) than the M1 (7YSZ) and even M2 (t' Low-k), and thus presents a very attractive replacement TBC material.
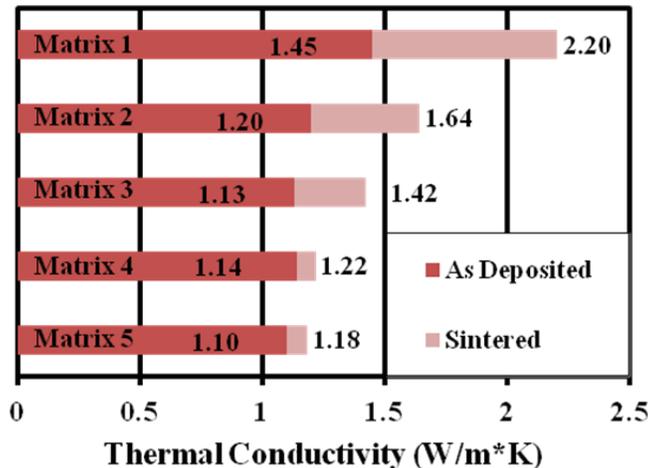
Figure 3.—Thermal conductivity of M1-M5 with initial values
plotted in the darker shade and values after 20 hr of
testing at 1316 °C surface temperatures plotted in the
lighter shade.

The erosion of coatings from Table 1 is presented in Figure 4 with SEM cross sections of M1-M3 shown in Figure 5. Focusing initially on the single layers (circles in Fig. 4), the first observation is that the M1 and M2 perform almost identically. When comparing Figures 5(a) and (b), we see minimal differences in the amount of plastic deformation and cracking at the TBC surface after erosion, indicating these materials behave very mechanically similar. According to Wellmann and Nicholls (Ref. 13), at particle velocities of 100 m/s and particle size of 50 μm we would expect to observe Mode I type damage. This is consistent with our observations in Figures 5(a) and (b) where the cracking is primarily limited to the first 5 to 10 μm with minimal plastic deformation. Since the rare earth elements have a very obvious impact on thermal properties, it is interesting that erosion remains almost identical. The overall stabilizer concentration was ~4 mol% in the t' Low-k coatings, which is very similar to the ~4 mol% Y_2O_3 in YSZ. According to the Shannon table (Ref. 14), the crystal radius of an eight coordinated Gd^{3+} is 1.193 Å while that of a similarly coordinated Yb^{3+} is 1.125 Å. The average of these is 1.159 Å, which is also the crystal radius of an eight coordinated Y^{3+}. Thus equimolar additions of Gd and Yb should have the same effect on lattice parameter as equivalent amounts of Y. This is important as the addition of Yb and Gd at the expense of Y will have minimal effects on the tetragonality, then the ferroelastic toughening (Ref. 15) should remain. One may surmise that additions of only rare earths with larger radii (such as Gd in our case) at the expense of Y would act to reduce the tetragonality, and diminish the ferroelastic toughening and thus erosion performance, though to the authors' knowledge there is no study relating the ionic radii, lattice parameter and subsequent toughness at a given concentration. The second important observation is that M3 has an erosion rate that is ~10 times higher than that of M1 and M2. The relatively low toughness of GZO results in a brittle material which readily fractures when impacted by erodent particles. Figure 5(c) shows significant fracture in the first 10 to 15 μm of the coating and with some even further down the columns (highlighted with arrows) leading to increased material loss. The morphology also plays a role, as larger column diameters tend to have high erosion rates (Ref. 16). In our case, the wider columns of M3 likely increase the erosion rate since a given spallation event of a fractured column results in more material loss. Also, there is minimal plastic deformation which means maximum energy is available for fracture. When combined with inherently low toughness, this results in a coating which exhibits a drastic reduction in erosion performance from current state of the art 7YSZ coatings such as M1. This is a major drawback of the GZO system and requires attention when considering the overall lifetime of the TBC system. One important consideration is that though the initial erosion rate of M3 may be relatively high compared to M1, in the aged condition the performance gap may be significantly smaller. This is due to the sintering rate of GZO being much lower than YSZ which yields minimal increases in erosion rate over

time, whereas YSZ has significant sintering and significant increases in erosion rate. M2 exhibits an erosion rate almost identical to that of YSZ and much lower than GZO in the as deposited condition. Therefore, in terms of coating life time, the t' Low-k system is favorable over GZO as it improves the thermal properties over YSZ without sacrificing erosion performance. The drawbacks to choosing t' Low-k over GZO are that GZO offers a higher maximum temperature capability, better thermal insulation and possible enhanced resistance to CMAS over t' Low-k. Thus, an ideal coating would combine these factors.
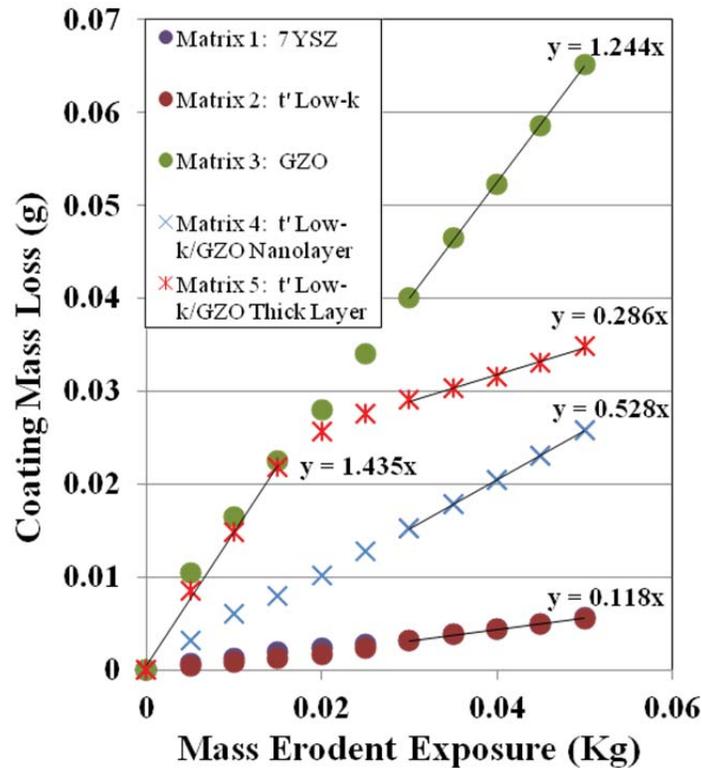
Figure 4.—Erosion data for M1-M5 with coating mass lass plotted as a function of erodent exposure. Erosion rates correspond to slopes of the lines and indicate that the nanolayer M4 is able to reduce the erosion rate with respect to M3 by ~57 percent.
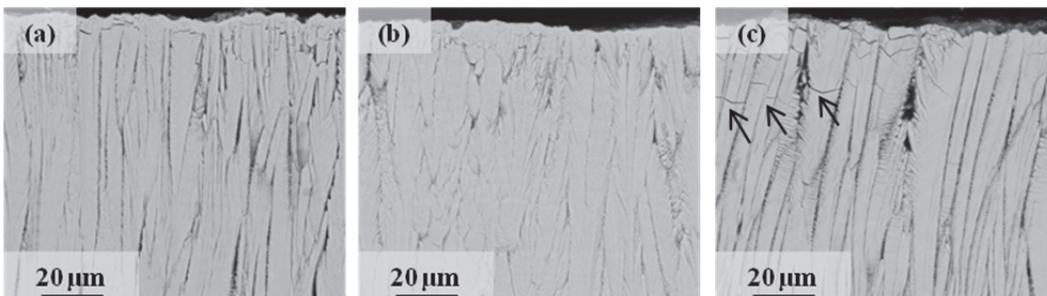
Figure 5.—SEM images of the polished cross sections after erosion testing for (a) M1 - YSZ, (b) M2 - t' Low-k, (c) M3 - GZO. Black arrows in (c) show where cracking has occurred at significantly lower depths than in (a) or (b).

Multilayer Coatings

Multilayer coatings composed of t' Low-k and GZO were deposited according to M4 (nanolayer) and M5 (thick layer) from Table 1 to combine the beneficial attributes of both classes of materials. M4 was deposited in an attempt to reduce the erosion rate with respect to GZO while maintaining a lower thermal conductivity relative to t' Low-k while M5 was deposited in order to study the effects of modifying layer thickness. SEM micrographs of M4 and M5 are presented in Figures 6(a) to (d), respectively. At a similar distance from the substrate, the column widths of M5 appear larger and denser than those of M4. The use of a single deposition ingot at a time reduces the deposition rate for M5 which in turn allows for increased surface adatom mobility and diffusion and therefore less nucleation of new columns. The higher magnification image of M4 in Figure 6(b) clearly illustrates the layered nature of the coating with individual layer thicknesses on the order of ~200 nm. This is increased to ~30 μm for the layers in M5. The diffraction patterns of M4 and M5 are presented in Figure 2. M4 is clearly a multiphase mixture of t' Low-k and cubic GZO as evidenced by the tetragonal (004) to (400) peaks and cubic (400) peak. The inset shows a reduction in the peak intensities and a 0.2° leftward shift of the tetragonal peaks to ~74° (004) and 73° (400) 2θ. The cubic (400) peak of GZO also shifts by ~0.2° to a position of 71.7 °2θ. There are several mechanisms that could be responsible for this shift. The layered nature of the coatings could cause CTE mismatch stresses, interface misfit stresses and intrinsic growth stresses. The CTE of YSZ is 10.7 ppm/K (Ref. 17) while GZO is 8.9 ppm/K (Ref. 18), the difference of which could cause stresses upon cooling. Likewise mismatch at the layer interfaces may cause misfit stresses, which, in conjunction with the relatively large interfacial volume, could have a significant contribution to the overall stress state. Crystallite size is also quite small in these coatings, as the layer thickness (~200 nm) limits grain size. This could also contribute to the overall stress state. We see a shift in the texturing from the {311} for the single layer coatings in M1-M3 to the {200} in M4. For M5, the diffraction pattern only shows evidence of the GZO phase, likely a product of its high absorption and the relatively large layer thickness. The coating is heavily textured in the {311} with no peaks visible in the tetragonal region (inset). This confirms the increased surface mobility mentioned previously.
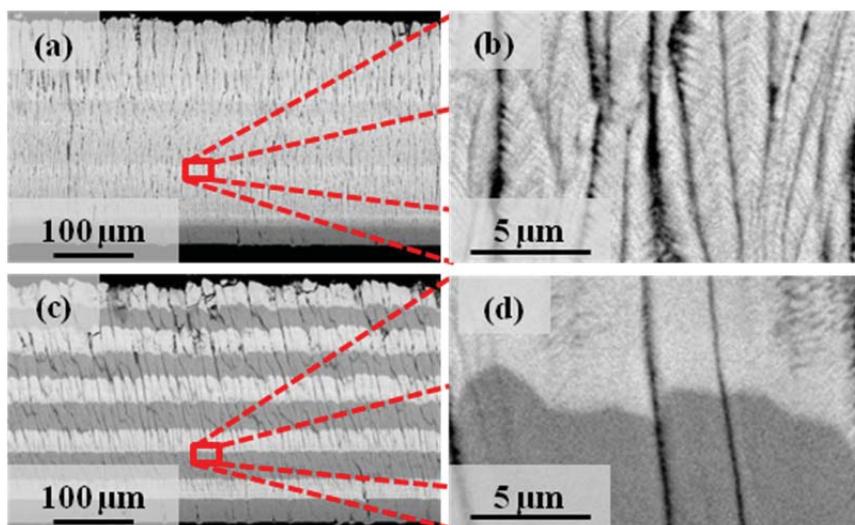
Figure 6.—SEM images of a polished cross section from the as deposited multilayered t' Low-k/GZO coatings with (a) showing the coating microstructure of M4, (b) showing a higher magnification view detailing the layered morphology of M4 and (c) showing the coating microstructure of M5, (d) showing a higher magnification image of one of the layer interfaces in M5.

The initial thermal conductivity of M4 is 1.14 W/m-K which increases by only 7 percent to 1.22 W/m-K after 20 hr (Fig. 3). The approximate composition of the coating is 50:50 t' Low-k: GZO. Equation (1) outlines a simple linear two phase mixing rule where P_x and P_y are the properties of interest for phase x and y, f_x and f_y are the phase fractions of phase x and y and P_c is the resulting property of the composite. Applying this mixing rule to thermal conductivity for our system, we would expect a conductivity of about 1.17 W/m*K for the nanolayer coating in M4.

$$P_c = P_x f_x + P_y f_y \tag{1}$$

The slight reduction in the observed thermal conductivity could be attributed to an increase in porosity and/or a morphology that more effectively scatters phonons. Hemispherical reflection has been shown to reduce phonon conduction in multilayer coatings (Ref. 19), but porosity must be consistent among coatings in order to confirm this effect. Since thermal conductivity is proportional to porosity, the 2 percent reduction in the observed thermal conductivity (1.14) from the expected value (1.17) would correspond to a 2 percent reduction in porosity. This is outside the accuracy of most image analysis software and most other common methods of analyzing TBC porosity, and thus we cannot confirm the presence of hemispherical reflection without further testing. The M5 coating yields a slight reduction in thermal conductivity to a value of 1.1 W/m-K. This decrease is likely a product of a combination of a slightly angled morphology and a lower coating density, though this is difficult to confirm. Interestingly, both coatings show an increase in thermal conductivity of ~7 percent over 20 hr. This is substantially less than the 37 and 26 percent increases observed for the parent phases M2 (t' Low-k) and M3 (GZO), respectively. If we again apply a rule of mixtures, we would expect an increase of ~32 percent increase. The observed 7 percent increase suggests there is very little sintering in the mutlilayer systems under these conditions. When comparing the multilayer coatings in M4 and M5 to the current state-of-the-art 7YSZ in M1, we observe a final thermal conductivity of almost half of M1's 2.2 W/m-K. This illustrates the enormous potential of the multilayer system.

From Figure 4, the erosion rate of M4 lies between that of M2 and M3. Thus, the layering of the tougher t' Low-k phase with the weak GZO phase is able to reduce the erosion rate with respect to GZO by 57 percent. If we apply the mixture rule to our erosion rate, we would expect a reduction of ~50 percent for a 50:50 mixture. The difference could be caused by changes in morphology, porosity, layer interfaces and strain state, among others. Again, this would require more analytical evaluation to extract the cause of the differences between expected and observed values. For M5, the initial erosion rate is 1.435 g/Kg, a value similar to that of M3-GZO. At 0.02 Kg of erodent fed, we observed a change in the slope to a value of 0.286 g/Kg which corresponds to a transition from the top GZO layer in the thick layer coating to the t' Low-k layer beneath. In this case the erosion rate of the t' Low-k layer in M5 is approximately twice that of pure t' Low-k in M2. There are several scenarios that could cause this, likely tied to the fact that though the t' Low-k layers in M5 are tough; the GZO layers below are quite weak. Post erosion SEM cross sections are presented in Figures 7(a) to (d). Figure 7(a) shows cracking primarily occurs in the top 10 μm for the coating from M4, very similarly to M1 and M2. On the other hand, there is almost no plastic deformation, similar to that observed in M3, which leads to some cracking at depths >10 μm as shown by the black arrow. This is further evidence of the combination of behaviors from both classes of materials. Figures 7(b) to (d) are SEM cross section images of the eroded sample from M5 at various locations along the surface. In the region of Figure 7(b) we see there is minimal cracking in the top t' Low-k layer yet there is significant cracking in the GZO layer beneath. This cracking can easily lead to large scale erosion of t' Low-k region when cracks begin to coalesce. Indeed, in a different region of the sample shown in Figure 7(c) we see significant interface cracking below the t' Low-k layer to the point that in part of the image the cracks have coalesced resulting in partial spallation and exposure of the next layer, GZO. Figure 7(d) shows an entire region where we have eroded completely through the t' Low-k layer and into the second GZO layer. Again, the only cracking that is observed occurs in the GZO layer. Interestingly, we can even observe fracture occurring below the t' Low-k layer in the next GZO layer (black arrows). Thus, it appears that crack initiation occurs almost exclusively in the GZO
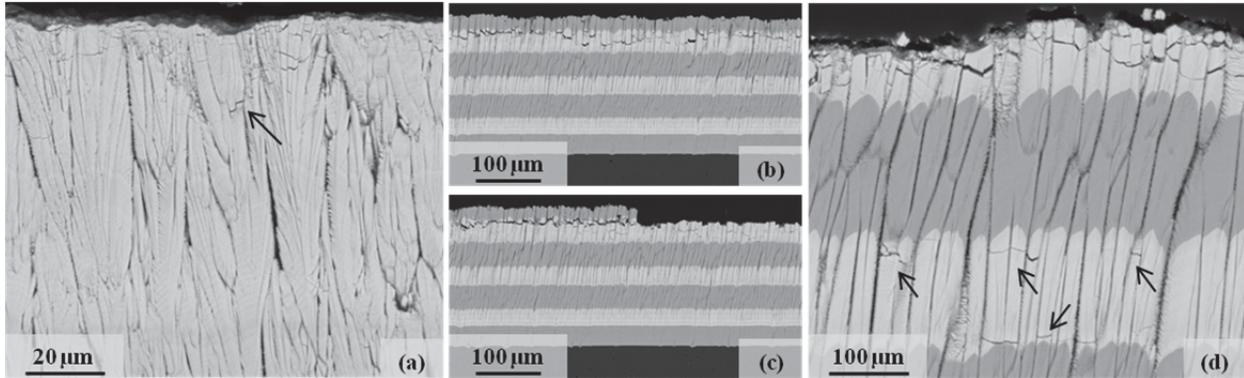
Figure 7.—SEM image of a polished cross section from the multilayered coatings from M4 (a) and three different regions along the surface of M5 (b-d) after erosion testing. Black arrows in (a) indicates where cracking has occurred at significantly lower depths than observed in for M1 or M2. In (b) the t' Low-k layer has been partially eroded with significant cracking occurring in the GZO layer below. In the region of (c), the cracks are beginning to coalesce which has lead to delamination of part of the t' Low-k layer. In (d), the t' Low-k layer has delaminated and the next GZO layer has been exposed and is severely cracked. Notably, no cracking occurs in the underlying t' Low-k layer but in the next GZO we see cracking (arrows).

layers and mostly near the layer interfaces and that it begins well before any erosion reaches the overlaying t' Low-k layer. This explains why the second slope observed was not as low as a pure t' Low-k layer, since some localized spallation occurs when sufficient cracks have been nucleated. Overall, the low erosion rate demonstrates that nanolayering GZO together with t' Low-k allows us to maintain much lower thermal conductivities and sintering rates as compared to 7YSZ and even t' Low-k single layers, while improving the erosion resistance with respect to GZO. Admittedly, a multiphase nanolayered TBC would add cost and complexity to the TBC manufacturing process but in critical components for high performance engines, there may be applicability. The thick layer coating exhibited similarly beneficial thermal performance but with a modified erosion mechanism which reduces overall performance.

Thermal Stability of Multilayer t' Low-k/GZO TBCs

The thermal stability of the multilayer systems were investigated via a series of isothermal heat treatments at 1316 °C. Figures 8(a) to (d) displays post heat treatment SEM image of M4 (a) and M5 (b) to (d) while Figure 9 details the corresponding pre and post heat treatment x-ray diffraction patterns for M4. The microstructures in Figure 8 all display the classical column sintering and densification with the feathery porosity coarsening into spherical pores. Of particular note though, is that the nanolayering is no longer evident for M4! This suggests there was significant interdiffusion between the layers during the heat treatment. From the diffraction pattern in Figure 9, it is immediately obvious that the nanolayer system has undergone a phase change. The three peaks (two split tetragonal peaks of the t' phase and a single cubic peak of the GZO phase) have merged into a single cubic peak at 72.7° 2θ. Interestingly, there is no evidence of any remaining t' or GZO peaks which indicates complete interdiffusion has occurred during the 20 hr heat treatment. This is ascribed to a compositional gradient that creates a thermodynamic driving force for interdiffusion which is exacerbated by a combination of non-homogenous layer thicknesses and non distinct layer interfaces. The nominal individual layer thickness is ~200 nm in these coatings, though this varies as a function of column inclination. A more detailed description of the process leading to this is given in Figure 10. This leads to areas where the layer thickness is approximately 50 nm which, even with small driving forces, may be too thin to prevent significant interdiffusion at 1316 °C. Secondly, TEM imaging and EDS mapping has indicated that the t' to GZO interface is relatively diffuse (Fig. 11). This is an artifact of the deposition process as complete separation of the vapor plumes is difficult and thus there is some degree of intermixing. As such, the diffuse
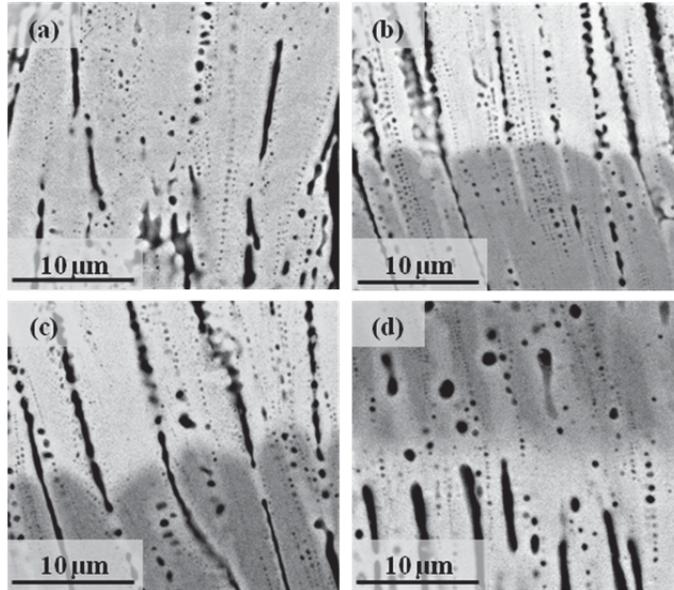
Figure 8.—SEM images of polished cross sections from M4 (a)
and M5 (b-d) after isothermal heat treatment at 1316 °C for
20 hr (a,b), 100 (c), and 500 (d) hr. The porosity has
spherodized for all coatings and the nanolayers are no longer
evident in the M4 coating. Diffusion progresses with time in
M5 and is extensive along the column boundaries.
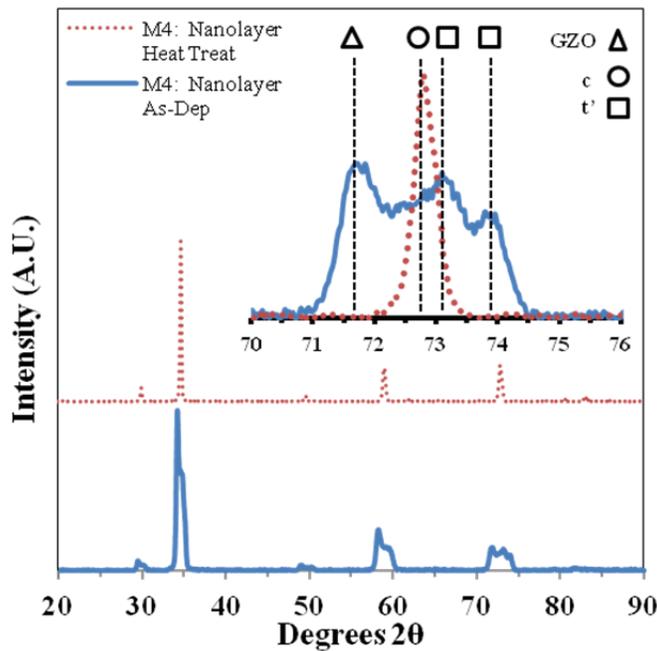
Figure 9.—X-ray diffraction patterns of as deposited (solid
line) and heat treated (dashed line) M4 with the high angle
(004)/(400) region inset. The mixed phase M4 transforms
into a single cubic phase after heat treatment, confirming
SEM observations of instability.
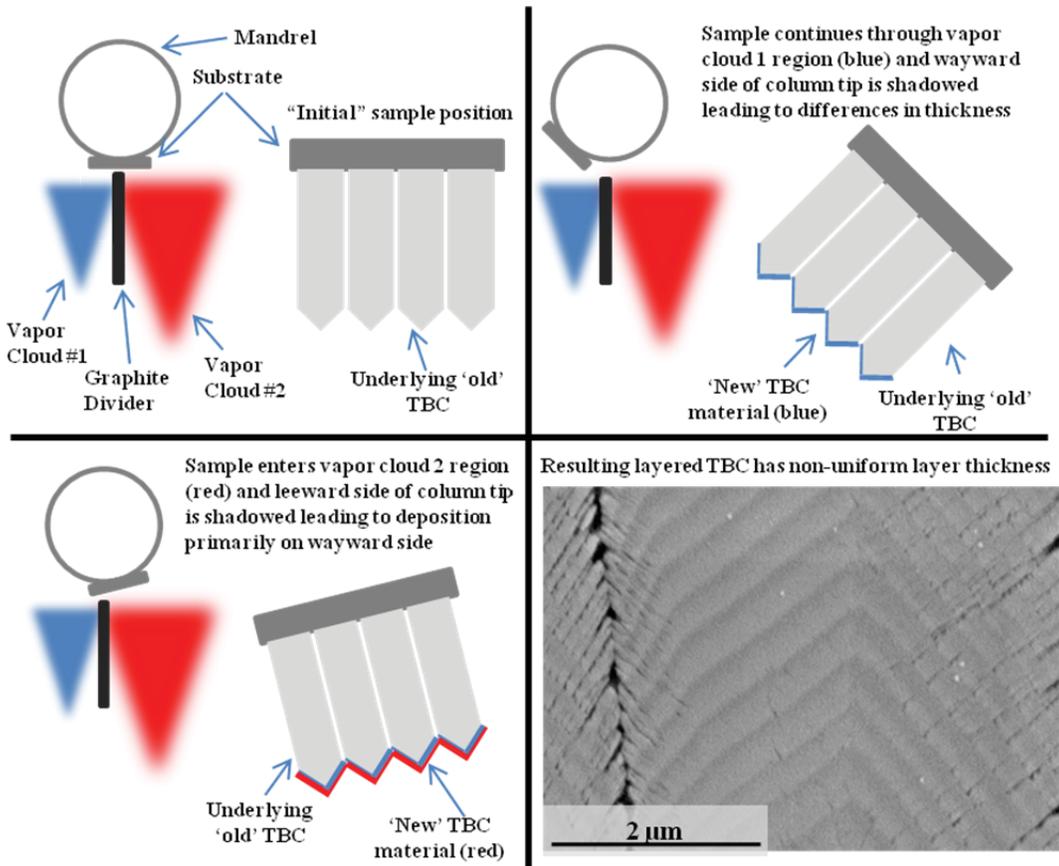
Figure 10.—Schematic showing the growth of the TBC when utilizing the co-deposition nanolayer setup. As the columns rotate over a given vapor cloud, part of the column surface is shadowed and so deposition is favored on a particular side of the column leading to non uniform layer thickness as shown in the micrograph on the bottom right.
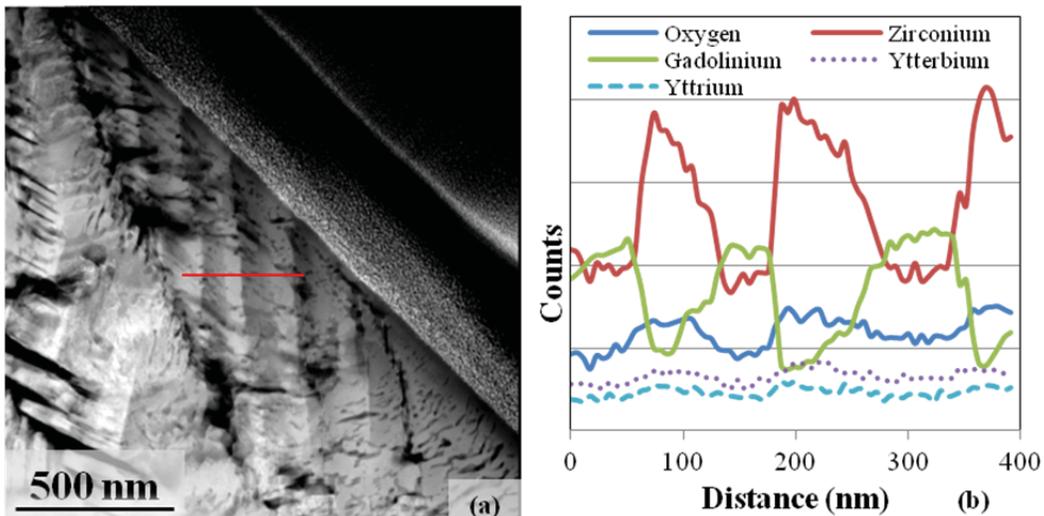
Figure 11.—TEM image (a) and EDS linescan (b) of a FIBed section from the cross section of M4. The red line represent the linescan region and corresponding EDS data suggests one of the interfaces is relatively diffuse while one is quite sharp. Coating growth direction is diagonally bottom right to top left.

interface likely creates some small volume that is cubic phase (but not GZO) even in the as-deposited state. This is not apparent in the as-deposited diffraction patterns, likely because the volume is quite small and the phase is so close in lattice parameter to GZO/t' (004) that it is very difficult to distinguish with a lab instrument. Interestingly, this interdiffusion does not appear to significantly reduce the lifetime of the coating. Initial thermal cycling results (55 min in, 5 min fan cooled) at ~1188 °C have shown that a standard 7YSZ and the GZO coating from M3 have the longest lifetimes of the single layer coatings. This cyclic life was matched by the nanolayer coating from M4 in our initial study. The durability of the thick layer coating, however, is markedly decreased and is currently being investigated. Since YSZ is typically used as a diffusion barrier to prevent GZO from reacting with Al_2O_3, the observed complete interdiffusion is troubling as formation of a high RE content cubic phase at the TBC/TGO interface must now be considered. If this phase has a RE content larger than some critical concentration X* (Ref. 9), it could potentially react with the TGO to form a perovskite (in the case of GZO) which will negatively affect the TBC adhesion.

The interaction of t' Low-k-GZO is more easily studied in the thick layer system from M5. Therefore, samples from M5 have also undergone heat treatments at 1316 °C for periods of 20, 100, and 500 hr with the corresponding SEM images presented in Figures 8(b) to (d), respectively. Notably, even at the 500 hr mark complete interdiffusion has not occurred in these samples. This confirms the complete phase change observed in the nanolayer system was primarily due to the layer thickness. From the 20 hr heat treatment image, we observe a ~0.5 μm interdiffusion region at the layer interfaces, well in excess of the ~200 nm layer thickness in the nanolayer system. This increases to ~1 μm in the case of the 100 hr treatment and >2 μm after 500 hr. These values help to establish an approximate diffusion path length which could assist in optimization of the layer thickness for future systems. In the ideal case, the layer thickness would be minimized such that the erosion either (a) exhibits a mechanism similar to M5 but removes much smaller amounts due to smaller layer thicknesses or (b) changes from a layer-by-layer mechanism to a standard sub-surface cracking as seen in M1-M4. This minimal layer thickness would be obtained by using the diffusion path lengths estimated from the current study. Notably, the diffusion extends along the column edges for ~5 μm in the 20 hr sample, and this gradually increases as heat treatment continues. This again brings up concerns of reactions with the TGO once the composition reaches X*.

Conclusions and Future Work

Thermal barriers composed of t' Low-k and GZO have been deposited and compared to standard 7YSZ in terms of thermal conductivity and erosion. While the GZO coating exhibited superb thermal conductivity and sintering resistance with respect to 7YSZ, the erosion rate increased by an order of magnitude. For design and lifetime considerations, this could preclude the use of GZO type coatings in certain areas of engine design. The t' Low-k materials exhibited an erosion rate nearly identical to YSZ yet with significantly better thermal conductivity. The multilayers of these two materials have been shown to reduce thermal conductivity and sintering rate to values very similar to GZO with only half the erosion debit of a pure GZO coating. Altering the layer thickness changes the erosion behavior due to the brittle nature of GZO which allows for sub surface layer cracking yielding a higher erosion rate in thicker layer coatings. It has been observed that the nanolayer system undergoes a phase change from a t'/cubic GZO mixture to a single cubic- fluorite phase which is attributed to a chemical potential gradient and layer thickness issue. There was still significant diffusion down the column edges in the thick layer system which indicates after long times and high temperatures, even a relatively thick diffusion layer may not sufficiently prevent GZO interaction with the TGO. This brings into question the long term suitability of Low-k YSZ as a diffusion barrier for GZO and other coatings with similar composition. The stability and interaction of GZO and YSZ/Low-k type coatings will be examined in greater detail in a forthcoming publication.

References

1. C.G. Levi, Emerging materials and processes for thermal barrier systems, Curr. Opin. Solid State Mater. Sci. 8 (2004) 77–91.
2. N. Mu, L. Izumi, B. Gleeson, The Development and Performance of Novel Pt+Hf-Modified γ′-Ni3Al+ γ-Ni Bond Coatings for Advanced Thermal Barrier Coating Systems, in: R.C. Reed, et al. (Eds.), Superalloys 2008, TMS, Champion, PA, 2008: pp. 629–637.
3. T. Izumi, N. Mu, L. Zhang, B. Gleeson, Effects of targeted γ-Ni+γ′-Ni3Al-based coating compositions on oxidation behavior, Surf. Coatings Technol. 202 (2007) 628–631.
4. R. Vassen, X. Cao, F. Tietz, D. Basu, D. Stover, Zirconates as New Materials for Thermal Barrier Coatings, J. Am. Ceram. Soc. 83 (2000) 2023–2028.
5. D. Zhu, Y.L. Chen, R.A. Miller, NASA/TM-2004-212480, NASA Glenn Research Center, Cleveland, OH, January 2004.
6. J. Wu, X. Wei, N.P. Padture, P.G. Klemens, M. Gell, P. Miranzo, et al., Low-Thermal-Conductivity Rare-Earth Zirconates for Potential Thermal-Barrier-Coating Applications, J. Am. Ceram. Soc. 85 (2002) 3031–3035.
7. D. Zhu, R.A. Miller, NASA/TM-2002-211481, NASA Glenn Research Center, Cleveland, OH, May 2002.
8. S. Krämer, J. Yang, C.G. Levi, Infiltration-Inhibiting Reaction of Gadolinium Zirconate Thermal Barrier Coatings with CMAS Melts, J. Am. Ceram. Soc. 91 (2008) 576–583.
9. R.M. Leckie, S. Krämer, M. Rühle, C.G. Levi, Thermochemical compatibility between alumina and ZrO2–GdO3/2 thermal barrier coatings, Acta Mater. 53 (2005) 3281–3292.
10. D.E. Wolfe, M.P. Schmitt, D. Zhu, A.K. Rai, R. Bhattacharya, Multilayered Thermal Barrier Coating Architectures for High Temperature Applications, in: D. Zhu et al. (Eds.), Adv. Ceram. Coatings Mater. Extrem. Environ., ACERS, Daytona, FL, 2013: pp. 3–18.
11. D. Zhu, R.A. Miller, B.A. Nagaraj, R.W. Bruce, Thermal conductivity of EB-PVD thermal barrier coatings evaluated by a steady-state laser heat flux technique, Surf. Coatings Technol. 138 (2001) 1–8.
12. D. Zhu, R.A. Miller, Thermal Conductivity and Elastic Modulus Evolution of Thermal Barrier Coatings under High Heat Flux Conditions, J. Therm. Spray Technol. 9 (2000) 175–180.
13. R.G. Wellman, J.R. Nicholls, A review of the erosion of thermal barrier coatings, J. Phys. D. Appl. Phys. 40 (2007) 293–305.
14. R.D. Shannon, Revised Effective Ionic Radii and Systematic Studies of Interatomie Distances in Halides and Chaleogenides, Acta Crystallogr. A32 (1976) 751–767.
15. C. Mercer, J. Williams, D. Clarke, A. Evans, On a ferroelastic mechanism governing the toughness of metastable tetragonal-prime (t′) yttria-stabilized zirconia, Proc. R. Soc. A. 463 (2007) 659–670.
16. R.G. Wellman, M.J. Deakin, J.R. Nicholls, The effect of TBC morphology on the erosion rate of EB PVD TBCs, Wear. 258 (2005) 349–356.
17. X.Q. Cao, R. Vassen, D. Stover, Ceramic materials for thermal barrier coatings, J. Eur. Ceram. Soc. 24 (2004) 1–10.
18. K.S. Lee, K.I. Jung, Y.S. Heo, T.W. Kim, Y.-G. Jung, U. Paik, Thermal and mechanical properties of sintered bodies and EB-PVD layers of Y2O3 added Gd2Zr2O7 ceramics for thermal barrier coatings, J. Alloys Compd. 507 (2010) 448–455.
19. D.E. Wolfe, J. Singh, R. a. Miller, J.I. Eldridge, D.-M. Zhu, Tailored microstructure of EB-PVD 8YSZ thermal barrier coatings with low thermal conductivity and high thermal reflectivity for turbine applications, Surf. Coatings Technol. 190 (2005) 132–149.